Influence of the oxidation on the optical properties of Mo-Si-Ti, Ta-Mo-Cr-Al and Ta-Mo-Cr-Ti-Al alloys

Ludovic Charpentier, Alexander Kauffmann, Eric Bêche, Christophe Escape, Stephan Laube, Daniel Schliephake, Jérôme Esvan, Bronislava Gorr, Audrey Soum-Glaude, Martin Heilmaier

Influence of the oxidation on the optical properties of Mo-Si-Ti, Ta-Mo-Cr-Al and Ta-Mo-Cr-Ti-Al alloys

L. Charpentier[1,*], A. Kauffmann[2], E. Bêche[1], C. Escape[1], S. Laube[2], D. Schliephake[2], J. Esvan[3], B. Gorr[2], A. Soum-Glaude[1], M. Heilmaier[2]

[1] PROMES-CNRS, 7 rue du Four Solaire, F-66120 Font-Romeu Odeillo, France

[2] Institute for Applied Materials (IAM), Karlsruhe Institute of Technology (KIT), Engelbert-Arnold-Straße 4, D-76131 Karlsruhe, Germany

[3] CIRIMAT-CNRS, 4 Allée Emile Monso, F-31400 Toulouse, France

Abstract. Three refractory element-based alloys were oxidized for 6 h at 1100 °C in air inside a muffle furnace and the way the oxidation, especially through the evolution of the surface composition and roughness, affects the optical properties of these materials is discussed here. The ternary Mo-20.0Si-52.8Ti (at.%) serves as an example of Mo-based alloys, while the equimolar Ta-Mo-Cr-Al (TMCA) and Ta-Mo-Cr-Ti-Al (TMCTA) are typical of the class of oxidation-resistant refractory compositionally complex alloys. The normal spectral emissivity of these three samples was increased due to the oxidation process. Oxidized TMCA and TMCTA exhibit a solar absorptivity higher than that of state-of-the-art Ni-based alloys used for solar receivers in concentrated solar power plants. Thus, the two refractory compositionally complex alloys are considered promising candidates for solar thermal energy conversion application.

Keywords. Alloy; XRD; Raman spectroscopy; XPS; Oxidation

1. Introduction

Solar thermal energy is an alternative to nuclear and non-renewable energies to generate heat and electricity with a reduced CO_2 footprint. Among them, systems that use a punctual focus on a receiver ensure the most effective conversion [1-2]. One of the major engineering barriers in the development of this category of these solar energy conversion systems is the maximum temperature at the receiver when directly exposed to air. The maximum operating temperature of the polycrystalline nickel-based alloys currently used in the design of industrial solar receivers is approximately 800 °C when 100,000 hours of use are considered [3]. In fact, previous investigations have revealed that Inconel 625 cannot withstand more than 36 h of exposure to air at 900 °C before oxide scale spallation occurs [4].

Apart from the failure of the oxides scales, high-temperature oxidation processes could limit the application by changing the surface spectral emissivity due to the growth of the oxides. Bulk TaC, for

* Corresponding author : ludovic.charpentier@promes.cnrs.fr, phone:+33 4 68 30 77 44, fax: +33 4 68 30 77 99

example, presents a high spectral emissivity in the range of the solar spectrum, maximizing its absorption, and a low spectral emissivity in the infrared spectrum, minimizing the thermal radiation losses. However, it has been previously demonstrated that these interesting radiative properties of TaC are seriously degraded during high-temperature oxidation due to Ta_2O_5 formation [5]. Besides the change in the surface composition, roughness evolution can also significantly affect the optical properties. As an example, Sciti *et al.* have evidenced how the surface patterning of hafnium or silicon carbides by femtolaser could increase the solar absorptivity and total emittance of the samples [6, 7]. Scratches and pores could generate multiple reflexions and interferences that would affect the radiative properties for the wavelengths inferior to their average size [8]. The mechanism behind the selectivity of textured surfaces has been investigated for some regular surfaces [9] such as:

- Vee corrugated specular surface: multiple reflexions on regular vee channels can improve the absorptance of the surface. A correlation was established between the opening angle of the vee channels and the absorptance, showing the absorptance is close to one for an opening angle of 20°, and decrease when this opening angle increases (up to 120 °) [10].
- Surface with regular square-sized holes: the absorptance a of one surface of copper (whose absortance for non-porous suface values $a_n = 0.15$) was calculated as a function of the fraction f of such holes in it and showed the absorptance of the porous surface followed a linear rule [11]: $a = a_n (1-f) + f$, approaching 1 when the material is highly porous.
- Denditric surfaces (on tungsten): A geometrical optical model was developed to adequately describe the multiple reflections from dendrites which have an average spacing of about 5 μm [12].

Hence, solar thermal energy conversion requires the formation of protective oxides (with a slow oxidation kinetics and consequently a minor surface evolution due to the oxide growth) with matching radiative properties.

Over the past decade, several refractory element-containing alloys with a promising resistance towards oxidation have been developed. In most cases, such alloys suffer from catastrophic oxidation phenomena, either by the formation of volatile oxides at intermediate temperatures between 500 and

900 °C, known as *pesting*, or voluminous oxides [13]. However, recent developments tackle this fundamental limitation as will be shown in the following.

The Mo-20.0Si-52.8Ti (in at.%) alloy (hereafter designated MST) undergoes a two-phase eutectic reaction to form a Mo-rich, body-centered (Strukturbericht designation A2) solid solution and a hexagonal, Mo-containing Ti_5Si_3 (Strukturbericht designation $D8_8$) silicide [14-16]. Specifically, in Mo-rich alloys, catastrophic failure at temperatures between 500 and 900 °C is caused by the formation and evaporation of volatile MoO_3. By forming a TiO_2 top layer with a TiO_2/SiO_2 duplex layer underneath, MST represents the first pesting-resistant alloy in air with high amounts of Mo-rich solid solution [14-16].

In contrast to this multi-phase MST alloy, an equimolar, Al-containing refractory compositionally complex Ta-Mo-Cr-Ti-Al (abbreviated TMCTA in what follows) alloy exhibits an ordered majority phase (Strukturbericht designation B2) with low amounts of Laves phase (Strukturbericht designation C14, Cr_2Ta-based) decoration at grain boundaries in the homogenized condition (at 1500 °C for 20 h) [17-19]. The absence of Ti in Ta-Mo-Cr-Al (TMCA) causes an increase in the volume fraction of the Laves phase and the formation of the Al-Mo-containing intermetallic phase (Strukturbericht designation A15) during the same homogenization treatment [18-19]. These novel alloys gain their excellent oxidation resistance from the formation of continuous complex rutile $(Cr,Ta,Ti)O_2$ oxide scales exhibiting low growth rates [19]. The present investigation aims at revealing the potential of these novel alloys for solar thermal energy conversion and the impact of oxidation on the optical properties of MST, TMCA and TMCTA. Through detailed characterization of the oxide scale and documentation of the surface roughness, indications of the oxide-phase specific improvement of the absorptivity are deduced.

2. Materials and methods

2.1. Sample preparation and oxidation

The alloys were manufactured by repetitive arc melting using an AM/0.5 device by Edmund Bühler GmbH, inside a water-cooled Cu crucible and under an Ar atmosphere at 0.6 bar. The metallic purities

of the different elements used in bulk form are 99.95% (Mo), 99.99% (Si), 99.8% (Ti), 99.9 % (Ta), 99 % (Cr) and 99.9% (Al). TMCA and TMCTA were subjected to a homogenization treatment at 1500 °C for 20 h under a flowing Ar atmosphere. A HTRT 70–600/18 tube furnace by Carbolite Gero GmbH & Co. KG was used at 100 K/h heating and cooling ramps. MST, TMCA and TMCTA samples were cut into disks with 25 mm and 2 mm in diameter and thickness, respectively, by electrical discharge machining.

One disk each was polished on one side to a mirror-finishing using a 1µm diamond paste (Struers A/S) and cleaned in an ultrasonic bath using ethanol following acetone. Initial optical measurements were performed on the polished surface. The samples were subsequently placed in a muffle furnace for 6 h in ambient air at 1100 °C to form an application-relevant oxide scale, and then cooled to room temperature in ambient atmosphere. The oxidized surface was analyzed by additional optical measurements on the polished oxidized surface. In parallel, another disk of each composition was cut into 5x5x2 mm^3 cuboid samples (two samples per composition) using a Buehler Isomet precision cutter. Each face of the samples was then polished following the same procedure as for the mirror-polished disk before and for each composition, one sample was kept as a reference and one was oxidized inside the muffle furnace using the same conditions as for the disk. The samples were placed on a wavy backing so that only two edges were in contact with the backing, the six faces of the cuboid being exposed to air. These oxidized cuboids were weighed before and after the oxidation directly using a microbalance (Ohaus) of ± 0.1 mg precision. The weight changes were divided by the total surface of the cuboids to normalized values for comparison [14-19].

2.2. Normal spectral emissivity measurement

Spectral emissivity was measured at room temperature using SOC (Surface Optic Corporation) 100 and PerkinElmer Lambda 950 devices. The PerkinElmer Lambda 950 is a laboratory two-beam scanning spectrophotometer that provides monochromatic light irradiance in the wavelength range of 175 – 3300 nm. In this investigation, a scan with 10 nm resolution was utilized. It is equipped with a 150 mm (diameter) integrating sphere and the hemispherical reflectance spectrum is obtained in the wavelength range between 250 and 2500 nm. The SOC 100 hemispherical directional reflectometer is

coupled to a Nicolet 6700 Fourier-transform infrared spectroscopy (FT-IR) spectrophotometer (supplied by ThermoFisher Scientific Inc.) for the 1.5 to 25 µm wavelength range. It provides hemispherical directional reflectance measurements at different detection angles from 8 to 80°. The reflectivity ρ was measured on both the setups for the four samples with 8° reflective angle, and the spectral emissivity $\varepsilon = 1 - \rho$ was calculated.

2.3. Characterization

Various surface analyses were performed to identify the surface changes due to the growth of the oxide scales. The evolution of the surface composition, crystallinity, chemical bonding and roughness are known as parameters that affect the optical properties [4, 5-8].

X-ray diffraction (XRD) was used to identify the crystalline compounds. XRD analyses were performed at room temperature using a PANalytical X'Pert Pro diffractometer (Cu-Kα radiation with $\lambda = 0.15418$ nm). The setup was θ-θ symmetric and the scans were performed over a 2θ range from 10 to 90°. The step size and the time per step were fixed at 0.017° and 50 s, respectively. The contribution of $CuK\alpha_2$ was removed (using the Rachinger method [20]).

Micro-Raman experiments were performed using a HORIBA LabRAM HR Evolution Raman spectrometer equipped with an optical microscope (Olympus K. K. BX 41, x10 Working Distance (WD), x50 (long working distance, LWD), x100 WD objective lens), a charge coupled device detector (1024 x 256 pixels, 26 x 26 μm^2 by pixel) and two laser beams (HeNe laser with a wavelength of 633 nm, laser power of 17 mW and laser diode with a wavelength of 532 nm, laser power of 39 mW). The Raman shift was calibrated using a Si standard sample. Measurements were performed at room temperature. Raman spectra were recorded in the wavenumber range (spectral region) from 150 to 1200 cm^{-1}. The excitation source is a 532 nm laser beam and the laser power was reduced to about 3.9 mW (90% filter strength) in order to avoid laser-induced effects (e.g. surface heating). No temperature effects (such as a shifting of the peaks or differences in the intensity ratios compared with reference spectra) were observed. The Raman spectra were collected at the focal point of the x50 objective lens (with a numerical aperture (NA) of 0.75) with a spectral resolution close to 1 cm^{-1}/pixel. The

1800 g/mm grating and the confocal pinhole value of 100 μm were selected. The acquisition time and the number of acquisitions per spectra were fixed to 5 s and 2, respectively. The Raman spectra were collected using the software delivered by HORIBA LabSpec 6.0.

X-ray photo-electron spectroscopy (XPS) analysis was performed using a K-Alpha™ X-Ray Photoelectron Spectrometer System by ThermoFisher Scientific. The XPS spectra were recorded using Al-Kα radiation (hν = 1486.6 eV) from a monochromatized source. The analyzed area was approximately 0.15 mm^2. The pass energy of the window scan was fixed at 30 eV. The spectrometer energy calibration was made using the Au $4f_{7/2}$ ((83.9 ± 0.1) eV) and Cu $2p_{3/2}$ ((932.8 ± 0.1) eV) photo-electron lines. XPS spectra were recorded in direct N(Ec). The atomic concentrations were determined with an accuracy of 8% from photoelectron peak areas using the atomic sensitivity factors reported by Scofield [21], taking into account the transmission function of the analyzer. This function was calculated at different pass energies from Ag 3d and Ag MNN peaks collected for a silver reference sample. The binding energy scale was established by referencing the C 1s value of adventitious carbon (284.8 eV [22]). The photoelectron peaks were analyzed by Gaussian/Lorentzian (G/L = 50) peak fitting. The background signal was removed using the Shirley method [23]. The depth of analysis of the XPS in such operating conditions is below 10 nm, giving the composition and chemical environment very close to the surface of the sample.

Surface roughness was measured using a Leica DCM 3D optical profile analyzer using the supplied x50 confocal objective lens. Five different surfaces (of length l and width L of 1 mm) are analyzed to obtain average values of the arithmetic (S_a) and quadratic (S_q) surface roughnesses and the corresponding standard deviations according to the procedure previously described [5].

3. Results

3.1. Optical measurements

After 6 h oxidation in air at 1100 °C, MST exhibits a slight mass loss of 0.25 mg cm^{-2}. TMCA and TMCTA gain 1.15 and 3.71 mg cm^{-2}, respectively. The normal spectral emissivity measured in the range of the solar spectral interval (0.25 - 4 μm) is presented in Figure 1 for the three samples and

compared with the spectral emissivity of Inconel 625 oxidized under the same conditions, whose spectral emissivity after oxidation has been published elsewhere [4]. All oxidized samples have spectral emissivities in the solar spectral interval higher than that of the polished samples. The oxidation of metallic substrates favors the absorption of the incident solar flux, which is favorable for the conversion of the concentrated flux into heat. The solar absorptivity α, calculated using equation (1), represents the ratio of the incoming solar flux absorbed by the surface of the sample. The integration has been performed numerically considering equidistant wavelength intervals:

$$\alpha = \frac{\int_0^{+\infty} \varepsilon(\lambda) \cdot I(\lambda)\, \mathrm{d}\lambda}{\int_0^{+\infty} I(\lambda)\, \mathrm{d}\lambda} \qquad (1)$$

In equation (1), ε and I are the spectral emissivity and solar irradiance at the wavelength λ, respectively. Figure 2 presents the solar absorptivity of the three alloys in the polished and oxidized condition in comparison to Inconel 625. The absorptivity of all samples and the Inconel reference sample increased subsequent to oxidation. Oxidized TMCTA possesses the highest α value, closely followed by oxidized TMCA. Only MST exhibits a solar absorptivity lower than Inconel 625.

3.2. Sample characterization

3.2.1. MST samples

Figure 3 presents the XRD diffraction patterns of MST samples post-oxidation. XRD analyses confirmed that the as-polished sample is composed of a body-centered cubic (Mo,Ti,Si) solid solution (A2, space group I m $\bar{3}$ m, no. 229) and of a hexagonal $(Ti,Mo)_5Si_3$ silicide ($D8_8$, space group P $6_3/$ m c m, no. 223) [14]. The phases detected on the oxidized samples are:

- rutile TiO_2 (space group P $4_2/$m n m, no. 136)
- minor amounts of α-cristobalite SiO_2 (space group P 4_1 2_1 2, no. 92)

Micro-Raman analyses are presented in Figure 4. The spectrum collected on the as-polished sample (Figure 4b) shows this sample is not Raman active, confirming the reference as metallic. In contrast, the micro-Raman spectrum acquired on the surface of the oxidized MST exhibits several bands located at about 142, 240, 440, 609, 695 and 830 cm^{-1}, attributed to a rutile TiO_2 compound [24-27].

The Raman spectra of rutile TiO_2 revealed four characteristic bands (one thin band and three wide bands):

- The thin Raman bands located at about 141-143 cm^{-1} are ascribed to the B_{1g} vibrations modes and are attributed to a combination of the bending of the O−Ti−O bonds.

- The wide Raman peak observed at about 235-240 cm^{-1} is ascribed to the second-order scattering effect (multi-phonon scattering process).

- The medium Raman peaks detected at about 440-445 cm^{-1} are assigned to the mixed E_g vibrations modes (bending of the O−Ti−O bonds).

- The strong Raman peaks detected at about 604-610 cm^{-1} are attributed to the mixed A_{1g} vibrations modes and are attributed to the stretching of the O−Ti−O bonds.

- The very weak and broad-band measured at about 830-837 cm^{-1} is ascribed to the B_{2g} vibrations modes (bending of the O−Ti−O bonds).

The key XPS results are presented in Table 1 and Figure 5. Table 1 presents the atomic composition that was measured on the oxidized surface of the MST. After oxidation, O is the predominant element on the surface of the samples (~ 70 at.%), followed by Ti (~ 13.8 at.%), Si (~ 12.5 at.%), and a minor amount of Mo (~ 3.7 at.%). Figure 5 presents the deconvolution of the O 1s photoelectron spectrum at the surface of the oxidized MST. The O 1s spectra were deconvoluted with three components, located at (532.8 ± 0.1), (530.8 ± 0.1), and (530.0 ± 0.1) eV. The first one can be attributed to O-Si bonds [22; 28-35] and minor O-C (from contamination). The shift between the O–Si and O–C components is less than 0.3 eV. Thus, in the peak-fitting process, only one component ((532.6 ± 0.1) eV) was used to identify these two types of bonds (O–C and O–Si). The component detected at (530.8 ± 0.1) eV is attributed to $O\text{-}Mo^{VI}$ bonds [22; 28; 36]. The component located at (530.0 ± 0.1) eV is assigned to $O\text{-}Ti^{IV}$ bonds [22; 28; 37]. Table 1 summarizes the position of the deconvoluted peaks for each element, their full width at half maximum (FWHM), the percentage of the bonds relative to the bonds involving the elements and the total number of bonds identified on the surface, and finally, the nature of the chemical bonds identified. The nature of the X-O bonds (where X is the metallic element) and the ratio

between X-O and O-X bonds allow the identification of the oxide phases present at the surface (information depth of maximum 10 nm) as TiO_2, SiO_2 and MoO_3, whose ratio in the analyzed area would be 46, 41.7 and 12.3 at.%, respectively.

Table 1. Main components positions and full width at half maximum (FWHM), percentage in the bonds related to the elements and the total amount of chemical bonds, and nature of the chemical bonds for the oxidized MST sample.

	O			Mo		Ti		Si	
	1s			$3d_{3/2}$	$3d_{5/2}$	$2p_{1/2}$	$2p_{3/2}$	$2p_{1/2}$	$2p_{3/2}$
Position (eV)	532.6	530.8	530.0	235.8	232.6	464.4	458.6	103.5	
FWMH (eV)	1.8	1.3	1.2	1.0	1.0	1.8	1.0	1.7	
%, element	38.4	16.8	44.8	39.7	60.3	33.5	66.5	100	
%, total	26.8	11.8	31.4	1.5	2.2	4.6	9.2	12.5	
Bonds	O-Si	O-Mo	O-Ti	Mo^{VI}-O	Mo^{VI}-O	Ti^{IV}-O	Ti^{IV}-O	Si^{IV}-O	

Figure 6 presents a surface profile obtained by optical roughness measurement on as-polished and oxidized samples, associated with the average value of the arithmetic Sa and quadratic Sq surface roughness measured on five different surfaces, with the corresponding standard deviations. A significant increase in surface roughness of one order of magnitude was observed during oxidation.

3.2.2. TMCA and TMCTA samples

XRD analyses on as-polished TMCA and TMCTA samples were published elsewhere [18] and confirmed in this study (not shown here). As-polished TMCA is B2 ordered with a significant amount of C14-type Laves phase (Cr_2Ta) and A15 phase ($AlMo_3$). As-polished TMCTA is B2 ordered with minor C14 Laves phase (Cr_2Ta).

XRD analyses on the oxidized TMCA and TMCTA (Figure 7) show the main differences between the two samples are due to the presence of Ti:

- Oxidized TMCA (Figure 7 a) presents major diffraction peaks assigned to a chromium tantalum oxide: tetragonal $CrTaO_4$ (ICDD 71-0931, space group P 4_2/m n m , no. 136). A slight peak asymmetry might be caused by the presence of an aluminum tantalum oxide: tetragonal $AlTaO_4$ (ICDD 76-1469, space group P 4_2/m n m, no. 136). Corundum α-Al_2O_3 (ICDD 76-7777, space group R $\bar{3}$ c, no. 167) and eskolaite Cr_2O_3 (ICDD 84-0313, space group R $\bar{3}$ c, no. 167) were also identified. β-Ta_2O_5 (ICDD 89-2843, space group C 2 m m, no. 38) was detected in minor amounts.
- Oxidized TMCTA (Figure 7 b) is mainly covered by a rutile TiO_2 (ICDD 79-6031, space group P 4_2/m n m , no. 136). Corundum α-Al_2O_3, Cr_2O_3 and shoulders at the TiO_2 peaks that can be attributed to $AlTaO_4$ and either $CrTaO_4$ or (Cr,Ta,Ti) O_2 phases (both compounds present diffraction peaks at similar positions [54]) were also identified. Two wide peaks are attributed to the TMCTA substrate beneath the oxide layers.

Polished TMCA and TMCTA samples are not Raman active. Oxidized TMCA (Figure 8) and TMCTA (Figure 9) present several active modes on their respective spectra, depending on the area of analysis.

Regarding oxidized TMCA, the spectra obtained on the global image (Figure 8 a-b) evidence vibrational modes at about 141, 302, 486, 676 and 808 cm^{-1} associated with the ones of Al-O bonds. Nevertheless, these are lower wavenumbers than the ones of pure Al_2O_3 [38-41]. These modes are attributed to Al_2O_3-based oxide solution. As shown in Figure 8 c, some yellow grains were observed on the surface of the sample. Point analyses on such a grain (Figure 8 d) revealed a new vibrational mode at 552 cm^{-1} that corresponds to a Cr_2O_3 compound [42-44].

Regarding oxidized TMCTA, the Raman peaks (Figure 9 b) collected for several acquisition points and detected at about 140, 248, 437 and 616 cm^{-1} are assigned to a rutile (TiO_2) compound. The Raman bands collected for several acquisition points and located at about 706 and 822 cm^{-1} are assigned to an oxide solution lean in Al. The Raman bands (Figure 9 d) collected on the yellow-white

regions are located at about 141, 181, 291, 412, 661, and 764 (741 to 779) cm^{-1}. These Raman band positions are similar to those observed for the TMCA sample.

Tables 2 and 3 and Figure 10 present the results of the XPS analyses performed on two different points on the surface of oxidized TMCA and TMCTA:

- Regarding the composition at the surface (information depth of maximum 10 nm) of the oxidized TMCA, Table 2 identifies O as the main element at the surface of the sample (55.8 at.% in point 1, 58.3 at.% in point 2), followed by Al (34.1 and 28.3 at.%), Cr (4.7 and 6.9 at.%), Mo (2.8 and 2.2 at.%) and Ta (2.6 and 3.5 at.%). According to these chemical compositions, the most intense peak observed at (530.8 ± 0.1) eV in the deconvolution of the O 1s peak (Figure 10 a) was mainly attributed to the presence of O-Al bonds [45-47]. The second most intense peak at (532.6 ± 0.1) eV corresponds to contaminations with O-C bonds. Comparing the two regions of analysis in Table 1, O-Al and Al-O bonds are in lower concentration in point 2 than in point 1. Point 2 is, however, enriched in Cr compared to point 1. If Al-O bonds correspond to Al_2O_3 compounds and Cr^{III}-O bonds to Cr_2O_3, the ratio between these two phases (calculated as the ratio between the total proportion of Al-O and Cr^{III}-O bonds) would be 7:1 in point 1, 4:1 in point 2.

Table 2. Main components positions and full width at half maximum (FWHM), the percentage in the bonds related to the elements and the total amount of chemical bonds, and the nature of the chemical bonds for oxidized TMCA samples, at two different locations.

	O		Ta		Mo		Cr		Al
Point 1	1s		$4f_{5/2}$	$4f_{7/2}$	$3d_{3/2}$	$3d_{5/2}$	$2p_{1/2}$	$2p_{3/2}$	$2p_{1/2,3/2}$
Position (eV)	532.6	530.8	27.8	25.9	235.7	232.6	586.7	576.8	74.3
FWMH (eV)	1.8	1.5	1.3	1.3	1.9	1.8	2.5	2.4	1.4
%, element	23.4	76.6	42.5	57.5	41	59	33	67	100
%, total	13.1	42.7	1.1	1.5	1.15	1.65	1.55	3.15	34.1
bonds	O-C	O-Al	Ta^{V}-O	Ta^{V}-O	Mo^{VI}-O	Mo^{VI}-O	Cr^{III}-O	Cr^{III}-O	Al-O
Point 2	1s		$4f_{5/2}$	$4f_{7/2}$	$3d_{3/2}$	$3d_{5/2}$	$2p_{1/2}$	$2p_{3/2}$	$2p_{1/2,3/2}$
Position (eV)	532.4	530.6	27.5	25.6	235.7	232.6	586.7	576.9	74.1
FWMH (eV)	1.8	1.5	1.3	1.3	1.9	1.8	2.6	2.5	1.5
%, element	21.6	78.4	43	57	41	59	33	67	100
%, total	12.8	46.3	1.5	2	0.9	1.3	2.3	4.6	28.3
bonds	O-C	O-Al	Ta^{V}-O	Ta^{V}-O	Mo^{VI}-O	Mo^{VI}-O	Cr^{III}-O	Cr^{III}-O	Al-O

- Regarding the composition at the surface of the oxidized TMCTA, Table 3 identifies O as the main element at the surface of the sample (62.9 at.% in point 1, 63 at.% in point 2), followed by Al (20.1 and 24.6 at.%), Ti (9.9 and 6.1 at.%), Mo (3.6 and 3.1 at.%) and Cr (3.2 and 3 at.%). Traces of Ta (below 0.2 at. %) are also reported. O 1s peak was deconvoluted into three components (see Figure 10 b-c): the one at (529.8 ± 0.1) eV, not present in Figure 10a corresponding to the TMCA sample, is attributed to the O-Ti bond [48-50]. According to previous Raman and XRD investigations, the corresponding compounds should be TiO_2. The contribution at (531.1 ± 0.1) eV is attributed to O-Al bonds. Compared with TMCA, this peak is slightly shifted from +0.3 eV. The last contribution at (532.6 ± 0.1) eV is ascribed to surface contamination (e.g., atmospheric C-H-based compounds) [51-52]. Comparing the two regions, it can be observed from Table 3 and Figure 10b and c that the O-Ti and Ti-O contributions are

more important in point 1 than in point 2. Al_2O_3 to TiO_2 ratio (calculated from the total proportions of Al-O to Ti-O bonds, taking into account two Al-O and one Ti-O bond are requested for the different compounds) values 1:1 in point 1, 2:1 in point 2.

Table 3. Main components positions and full width at half maximum (FWHM), the percentage of the bonds related to the elements and the total amount of chemical bonds, and the nature of the chemical bonds for oxidized TMCTA samples, at two different locations.

	O			Ta		Mo		Cr		Ti		Al
Point 1	1s			$4f_{5/2}$	$4f_{7/2}$	$3d_{3/2}$	$3d_{5/2}$	$2p_{1/2}$	$2p_{3/2}$	$2p_{1/2}$	$2p_{3/2}$	$2p_{1/2,3/2}$
Position (eV)	532.5	531.1	529.8	27.5	25.6	235.65	232.5	586.7	576.8	464.18	458.26	74.3
FWMH (eV)	1.8	1.5	1.4	0.95	0.95	1.6	1.6	2.6	2.5	1.85	1.02	1.4
%, element	6.1	52.8	41.1	/	/	39.4	60.6	33	67	33.5	66.5	100
%, total	3.8	33.3	25.9	0.1		1.4	2.2	1.05	2.15	3.3	6.6	20.1
bonds	O-C	O-Al	O-Ti	Ta^{V}-O	Ta^{V}-O	Mo^{VI}-O	Mo^{VI}-O	Cr^{III}-O	Cr^{III}-O	Ti^{IV}-O	Ti^{IV}-O	Al-O
Point 2	1s			$4f_{5/2}$	$4f_{7/2}$	$3d_{3/2}$	$3d_{5/2}$	$2p_{1/2}$	$2p_{3/2}$	$2p_{1/2}$	$2p_{3/2}$	$2p_{1/2,3/2}$
Position (eV)	532.6	531.1	529.8	27.6	25.7	235.8	232.65	586.8	576.9	464.3	458.4	74.4
FWMH (eV)	1.7	1.5	1.3	1	1	1.6	1.6	2.65	2.6	1.85	1.02	1.4
%, element	6.2	61.7	32.1	/	/	39.4	60.6	33	67	33.6	66.4	100
%, total	3.9	38.9	20.2	0.2		1.2	1.9	1	2	2.05	4.05	24.6
bonds	O-C	O-Al	O-Ti	Ta^{V}-O	Ta^{V}-O	Mo^{VI}-O	Mo^{VI}-O	Cr^{III}-O	Cr^{III}-O	Ti^{IV}-O	Ti^{IV}-O	Al-O

Figure 11 presents a characteristic surface profile obtained by optical roughness measurement on as-polished and oxidized samples, associated with the average value of the arithmetic Sa and quadratic Sq surface roughnesses measurements from five different locations on the surfaces, with the corresponding standard deviations. Contrary to the MST samples, it is impossible to polish TMCA and TMCTA samples up to submicron roughnesses due to the selective removal of grains and the presence of porosity from the synthesizing by repetitive arc melting. We can observe the oxidation results in surface modification with a rougher aspect of the oxidized surface.

4. Discussion

The composition of the oxide layer grown on the MST samples is consistent with the previous results

on samples oxidized for up to 100 h at 800, 1100 or 1200 °C [14-16]. In these previous works, a slight, througthout positive mass gain of only 0.5 and 1.3 mg/cm² was detected during cyclic and isothermal oxidation, respectively, at 1100 °C after 6 h. A formation of an oxide layer consisting of a mixture of SiO_2-TiO_2 covered with TiO_2 (rutile being the only crystalline compound identified using electron backscatter diffraction [14]) was revealed. The main difference between our results and the published observations [13-14] is that we observed a slight mass loss. This may be due to a more pronounced formation of volatile MoO_3 during this 6 h oxidation period. It has to be noted that in general the mass changes are small and, thus, are influenced by the distinct experimental setup, namely edge-to-surface ratio of the sample geometry and gas supply which are different for the three setups in comparison. XPS has identified a small amount of MoO_3 (12.3 at.%) on the surface of the sample; since this compound has not been identified by XRD or Raman, this presence is probably due to condensation of MoO_3 vapor during the cooling of the sample. The predominant compound on the oxidized surface is rutile TiO_2. XPS determined its content to be ~ 46 at.%. This rutile forms together with SiO_2 in a proportion of 41.7 at.%. Cristobalite peaks appear in the X-ray diffraction pattern. Nevertheless, their intensities are much lower than those of rutile, additionally, the Raman analyses did not show the presence of crystalline Si-O bonds. These results are consistent with the previously reported scale models for MST with TiO_2 top layers and TiO_2/SiO_2 duplex layers underneath. The SiO_2 is mostly present in an amorphous form.

The oxidation mechanism of TMCA and TMCTA has previsously been studied at temperatures ranging from 900 to 1500 °C [18-19; 53]. Müller *et al.* [18] reported changing oxidation kinetics during thermogravimetric oxidation at 1000 °C for both alloys. TMCTA exhibits a quartic oxidation rate law following a parabolic initial period. After about 6 h of exposure, a mass gain of approximately 1.4 mg/cm² was detected. For oxidation at 1100 °C, this does not change significantly. In TMCA, the behavior is opposite with an initial quartic behavior and a transition to parabolic. After 6 h of oxidation, a marginal mass gain of only 0.2 mg/cm² was reported. In TMCTA the oxide scale was found to consist of several layers with an intermediate $(Cr,Ta,Ti)O_2$ phase whereas TMCA presents an

intermediate $CrTaO_4$ layer [54]. The $(Cr,Ta,Ti)O_2$ or $CrTaO_4$ are covered by different oxides according to the initial composition:

- The upper layer of the oxide grown on TMCA samples is composed of a mixture of Al_2O_3 and Cr_2O_3.
- The upper layer of the oxide grown on TMCTA samples constitutes rutile TiO_2 covering an intermediate layer of Al_2O_3 and Cr_2O_3. Schellert *et al.* [19] have shown the formation of the oxide layer formed after 24h oxidation at 1200 °C was similar.

Our work has also identified an intermediate $CrTaO_4$ or $(Cr,Ta,Ti)O_2$ layer on TMCA and TMCTA samples using XRD. Shouldering was identified due to the presence of $AlTaO_4$ as a minor phase in this layer. XRD also identified Al_2O_3 (as corundum) and Cr_2O_3 (as eskolaite) at the surface of both samples, whereas the diffraction patterns of TMCTA show significant peaks of TiO_2 (as a rutile phase). Micro-Raman and XPS analyses (whose depth resolution is less than 10 nm) identify the proportions of these three phases close to the surface of the sample:

- TMCA is mainly covered with Al_2O_3 phase. XPS identifies this phase as the predominant one, followed by Cr_2O_3. Micro-Raman analysis coupled with optical microscopy reveals that the Cr_2O_3 is present as yellow grains on a surface otherwise mainly composed of aluminium oxide. Nevertheless, the vibrational modes of the Al-O bonds in the micro-Raman spectra and the position of the contribution of O-Al bonds in the XPS spectra (at (530.7 ± 0.1)eV) are shifted with respect to the theoretical values corresponding to pure corundum (XPS detects the O-Al bonds at (531.3 ± 0.1) eV for such a pure phase), indicating that there should be some inclusions of other metallic elements in this Al_2O_3 phase.
- TMCTA is mainly covered with rutile TiO_2 and Al_2O_3. In the XPS spectra of TMCTA, the O-Al bond contribution is located at (531.1 ± 0.1) eV, which means that the Al_2O_3 phase covering TMCTA should be closer to impurity-lean corundum than the one grown on TMCA. The weak signals registered in the Micro-Raman spectra may be due to the fact that Al_2O_3 is significantly covered by rutile.

Regarding the optical properties, the oxide species that will make up the top surface of the oxidized samples will therefore be SiO_2 and TiO_2 (MST), Al_2O_3 and Cr_2O_3 (TMCA), Al_2O_3 and TiO_2 (TMCTA), the latter being the combination with the highest solar absorptivity. The formation of each of these oxides can increase the solar absorptivity of the substrate. Colas *et al.* [4] observed this improvement due to the growth of Cr_2O_3 on Inconel. Arena *et al.* [55] reported that the formation of rutile TiO_2 had a positive effect on the optical properties of TiC-SiC composite ceramics. One of our recent investigations [56] also reported that amorphous SiO_2 grown on SiC coatings can have a positive impact on the optical properties due to the transparency of the oxide layers, which generates multiple reflections and interferences within the oxide layer.

Figure 12 presents the normal spectral reflectance curves in the solar spectral region of SiO_2 (polycrystalline), TiO_2 (rutile), Al_2O_3 (polycrystalline) and Cr_2O_3 (polycrystalline) at room temperature extracted from literature [57]. TiO_2 exhibits the lowest reflectance, followed by Cr_2O_3. Polycrystalline Al_2O_3 and SiO_2 possess higher reflectance values. Nevertheless, vitreous silica has a reflectance below 0.1 in the solar spectrum range and is transparent in this wavelength interval (with $\tau > 0.9$) [57]. Crystalline alumina alsor presents high transmittance (with $\tau > 0.8$) in this interval [57]. Translating these observations to the oxide composition at the surface of the sample:

- MST forms an oxide layer whose surface is composed of TiO_2 + SiO_2, the latter being crystallized only to a small extent. The presence of TiO_2 can explain why the oxidized sample presents a higher solar absorptivity value than the as-polished sample. The significant increase in roughness due to the outward growth of TiO_2 can also be a second cause for the modification of the optical properties as previously observed [51]. Nevertheless, the oxidized MST does not exhibit a higher solar absorptivity than oxidized Inconel [4].
- TMCA presents an oxide layer mainly made of Al_2O_3 with Cr_2O_3. Cr_2O_3 is a component of lower reflectance than Al_2O_3, which can increase solar absorptivity. According to Raman and XPS spectra, Cr_2O_3 grains seem to cover the Al_2O_3 layer whose semi-transparency can enhance the absorptivity through reflections and intereferences as previously observed [56].

This can explain why the oxidized TMCA (covered by a mixture of Cr_2O_3 + Al_2O_3) presents an higher spectral emissivity than the oxidized Inconel 625 (mainly covered by Cr_2O_3).

- The growth of rutile TiO_2 on the surface of the oxidized TMCTA covering Al_2O_3 can explain why this alloy has the highest value of solar absorptivity among the three investigated alloys, even higher than that of oxidized Inconel 625.

5. Conclusion

These investigations correlate the previously identified oxidation mechanisms of Mo-Si-Ti, Ta-Mo-Cr-Al and Ta-Mo-Cr-Ti-Al alloys with their optical performance depending on the surface condition, before and after oxidation. A positive influence of the formation of Cr_2O_3 and/or TiO_2 compounds on the surface is identified with respect to the solar absorptivity in the oxidized state of all three samples. Ta-Mo-Cr-Al and Ta-Mo-Cr-Ti-Al exhibit higher solar absorptivity than the currently used Inconel 625. Adjusting the composition of these two alloys away from equimolar to promote the formation of the less reflective oxides without compromising oxidation resistance may be a way to produce compositions with improved potential for solar applications.

Acknowledgements

This work was supported by the French "Investments for the future" program, funded by the French National Research Agency (ANR) under contracts ANR-10-LABX-22-01-SOLSTICE and ANR-10-EQPX-49-SOCRATE. This work was financially supported by the Deutsche Forschungsgemeinschaft (DFG), grant no. HE 1872/34-2 and HE 1872/38-1.

References

[1] R. Pitz-Paal, 19 - Concentrating Solar Power, in: T. M. Letcher (Ed.), Future Energy: Improved, Sustainable and Clean Options for Our Planet, Third Edition, Elsevier Ltd, Amsterdam, 2021, pp. 413-430. https://doi.org/10.1016/B978-0-08-102886-5.00019-0

[2] C. A. Schoeneberger, C. A. McMillan, P. Kurup, S. Akar, R. Margolis, E. Masanet, Solar for industrial process heat: A review of technologies, analysis approaches, and potential applications in the United States, Energy 206 (2020) 118083. https://doi.org/10.1016/j.energy.2020.118083

[3] J. A. Siefert, C. Libby, J. Shingledecker, Concentrating solar power (CSP) power cycle improvements through application of advanced materials, AIP Conf. Proc. 1734 (2016) 070030. https://doi.org/10.1063/1.4949177

[4] J. Colas, L. Charpentier, M. Balat-Pichelin, Oxidation in air at 1400 K and optical properties of Inconel 625, FeCrAlloy and Kanthal Super ER, Oxid. Met. 93 (2020) 355-370. https://doi.org/10.1007/s11085-020-09959-6

[5] L. Charpentier, C. Caliot, The impact of the oxidation on the optical properties of TaC, Sol. Energ. Mat. Sol. C. 171 (2017), 16-23. https://doi.org/10.1016/j.solmat.2017.06.019

[6] D. Sciti, L. Silvestroni, D.M. Trucchi, E. Cappelli, S. Orlando, E. Sani, Femtosecond laser treatments to tailor the optical properties of hafnium carbide for solar applications, Sol. Energ. Mat. Sol. C. 132 (2015), 460-466. http://dx.doi.org/10.1016/j.solmat.2014.09.037

[7] D. Sciti, D.M. Trucchi, A. Bellucci, S. Orlando, L. Zoli, E. Sani, Effect of surface texturing by femtosecond laser on tantalum carbide ceramics for solar receiver applications, Sol. Energ. Mat. Sol. C. 161 (2017), 1-6. http://dx.doi.org/10.1016/j.solmat.2016.10.054

[8] H. Aréna, M. Coulibaly, A. Soum-Glaude, A. Jonchère, A. Mesbah, G. Arrachart, N. Pradeilles, M. Vandenhende, A. Maitre, X. Deschanels, SiC-TiC nanocomposite for bulk solar absorbers applications: Effect of density and surface roughness on the optical properties, Sol. Energ. Mat. Sol. C. 191 (2019) 199-208. https://doi.org/10.1016/j.solmat.2018.11.018

[9] G. Pellegrini, Experimental methods for the preparation of of selectively absorbing textured surfaces for photothermal solar conversion, Sol. Energ. Mater. 3 (1980) 391-404. https://doi.org/10.1016/0165-1633(80)90028-3

[10] K. G. T. Hollands, Directional selectivity, emittance and absorptance properties of vee corrugated specular surfaces, Sol. Energy 7 (1963) 108-116. https://doi.org/10.1016/0038-092X(63)90036-7

[11] C. M. Horwitz, A new solar selective surface, Opt. Commun. 11 (1974) 210-212. https://doi.org/10.1016/0030-4018(74)90223-5

[12] T. H. DiStefano, G. D. Pettit, A. A. Levi, The reflectance of dendritic- tungsten surfaces, J. Appl. Phys. 50 (1979) 4431-4435. https://doi.org/10.1063/1.326435

[13] B. Gorr, S. Schellert, F. Müller, H.-J. Christ, A. Kauffmann, M. Heilmaier, Current status of research on the oxidation behavior of refractory high entropy alloys, Adv. Eng. Mater. 23 (2021) 2001047. https://doi.org/10.1002/adem.202001047

[14] D. Schliephake, A. Kauffmann, X. Cong, C. Gombola, M. Azim, B. Gorr, H.J. Christ, M. Heilmaier, Constitution, oxidation and creep of eutectic and eutectoid Mo-Si-Ti alloys, Intermetallics 104 (2019) 133-142. https://doi.org/10.1016/j.intermet.2018.10.028

[15] S. Obert, A. Kauffmann, M. Heilmaier, Characterisation of the oxidation and creep behaviour of novel Mo-Si-Ti alloys, Acta Mater. 184 (2020) 132-142. https://doi.org/10.1016/j.actamat.2019.11.045

[16] S. Obert, A. Kauffmann, S. Sails, S. Schellert, M. Weber, B. Gorr, H.J. Christ, M. Heilmaier, On the chemical and microstructural requirements for the pesting-resistance of Mo-Si-Ti alloys, J. Mater. Res. Technol. 9 (2020) 8556-8567. https://doi.org/10.1016/j.jmrt.2020.06.002

[17] H. Chen, A. Kauffmann, S. Seils, T. Boll, C.H. Liebscher, I. Harding, K.S. Kumar, D.V. Szabó, S. Schlabach, S. Kauffmann-Weiss, F. Müller, B. Gorr, H.-J. Christ, M. Heilmaier, Crystallographic ordering in a series of Al-containing refractory high entropy alloys Ta-Nb-Mo-Cr-Ti-Al, Acta Mater. 176 (2019) 123-133. https://doi.org/10.1016/j.actamat.2019.07.001

[18] F. Müller, B. Gorr, H. J. Christ, J. Müller, B. Butz, H. Chen, A. Kauffmann, M. Heilmaier, On the oxidation mechanism of refractory high entropy alloys, Corros. Sci. 159 (2019) 108161. https://doi.org/10.1016/j.corsci.2019.108161

[19] S. Schellert, B. Gorr, S. Laube, A. Kauffmann, M. Heilmaier, H. J. Christ, Oxidation mechanism of refractory high entropy alloys Ta-Mo-Cr-Ti-Al with varying Ta content, Corros. Sci. 192 (2021) 109861. https://doi.org/10.1016/j.corsci.2021.109861

[20] W.A. Rachinger, A correction for the α1 α2 doublet in the measurement of widths of X-ray diffraction lines, J. Sci. Instrum. 25 (1948), 254. https://doi.org/10.1088/0950-7671/25/7/125

[21] J.H. Scofield, Hartree-Slater subshell photoionization cross-sections at 1254 and 1487 eV, J. Electron Spectrosc. 8 (1976) 129-137. https://doi.org/10.1016/0368-2048(76)80015-1

[22] M.P. Seah, Practical Surface Analysis, second ed., J. Wiley & Sons, New York, 1993.

[23] D.A. Shirley, High-resolution X-ray photoemission spectrum of the valence bands of gold, Phys. Rew. B 5 (1972) 4709-4714. https://doi.org/10.1103/PhysRevB.5.4709

[24] H.L. Ma, J.Y. Yang, Y. Dai, Y.B. Zhang, B. Lu, G.H. Ma, Raman study of phase transformation of TiO_2 rutile single crystal irradiated by infrared femtosecond laser, Appl. Surf. Sci. 253 (2007) 7497-7500. https://doi.org/10.1016/j.apsusc.2007.03.047

[25] Y.H. Zhang, C.K. Chan, J.F. Porter, W. Guo, Micro-Raman spectroscopic characterization of nanosized TiO_2 powders prepared by vapor hydrolysis, J. Mater. Res. 13 (1998) 2602-2609. https://doi.org/10.1557/JMR.1998.0363

[26] O. Secundino-Sanchez, J. Diaz-Reyes, J.F. Sanchez-Ramırez, J.L. Jimenez-Perez, Structural and optical characterization of the crystalline phase transformation of electrospinning TiO_2 nanofibres by high-temperatures annealing, Rev. Mex. Fis. 65 (2019) 459-467. https://doi.org/10.31349/RevMexFis.65.459

[27] L. Palliyaguru, U.S. Kulathunga, L.I. Jayarathna, C.D. Jayaweera, P.M. Jayaweera, A simple and novel synthetic route to prepare anatase TiO_2 nanopowders from natural ilmenite via the H_3PO_4/NH_3 process, Int. J. Miner. Metall. Mater., 27 (2020) 846-855. https://doi.org/10.1007/s12613-020-2030-3

[28] J.F. Moulder, W.F. Stickle, P.E. Sobol, K.D. Bomben, Handbook of X-ray Photoelectron Spectroscopy, Physical Electronics Division, Perkin-Elmer Corporation, Eden Prairie, MN, 1995.

[29] S. Scordo, M. Ducarroir, E. Bêche, R. Berjoan, On the nature of microwave deposited hard silicon-carbon films J. Mater. Res. 13 (1998) 3315-3325. https://doi.org/10.1557/JMR.1998.0451

[30] N. Nakamura, K. Hirao, Y. Yamauchi, Surface analytical studies of ion-implanted uni-directionally aligned silicon nitride for tribological applications, Nucl. Intrum. Meth. Phys. Res. B 217 (2004) 51-59. https://doi.org/10.1016/j.nimb.2003.09.024

[31] J. Eck, M. Balat-Pichelin, L. Charpentier, E. Bêche, F. Audubert, Behavior of SiC at high temperature under helium with low oxygen partial pressure, J. Eur. Ceram. Soc. 28 (2008) 2995-3004. https://doi.org/10.1016/j.jeurceramsoc.2008.04.032

[32] J. Pourasad, N. Ehsani, S. A. Khalifesoltani, Preparation and characterization of SiO_2 thin film and SiC nanofibers to improve of graphite oxidation resistance, J. Eur. Ceram. Soc. 36 (2016) 3947-3956. https://doi.org/10.1016/j.jeurceramsoc.2016.06.046

[33] M.S. Chandrasekar, N.R.Srinivasan, Role of SiO_x on the photoluminescence properties of β-SiC, Ceram. Int. 42 (2016) 8900-8908. https://doi.org/10.1016/j.ceramint.2016.02.145

[34] Z. Zhang, C. Nan, J. Xu, Z. Gao, M. Li, J. Wang, Oxidation Behaviors of C–ZrB_2–SiC Composite at 2100 °C in Air and O_2, J. Mater. Sci. Technol. 30 (2014) 1223-1229. https://doi.org/10.1016/j.jmst.2014.04.013

[35] E. Beche, M. Balat-Pichelin, V. Flaud, J. Esvan, T. Duguet, D. Sciti, D. Alfano, XPS and AES studies of UHTC ZrB_2–SiC–Si_3N_4 treated with solar energy, Surf. Interface Anal. 46 (2014) 817–822. https://doi.org/10.1002/sia.5389

[36] M. Nayak, G.S. Lodha, R.V. nandedkar, S.M. Chaudhari, P. Bhatt, Interlayer composition in Mo-Si multilayers using X-ray photoelectron spectroscopy, J. Electron Spectrosc. 152 (2006) 115-120. https://doi.org/10.1016/j.elspec.2006.04.005

[37] M. C. Biesinger, L. W. M. Lau, A. Gerson, R. St. C. Smart, Resolving Surface Chemical States in XPS Analysis of First Row Transition Metals, Oxides and Hydroxides: Sc, Ti, V, Cu and Zn, Appl. Surf. Sci. 257 (2010) 887-898. https://doi.org/10.1016/j.apsusc.2010.07.086

[38] S.P.S. Porto, R.S. Krishnan, Raman Effect of Corundum, J. Chem. Phys. 47 (1967) 1009. https://doi.org/10.1063/1.1711980

[39] J.A. Xu, E. Huang, J.-F. Lin, L.Y. Xu, Raman study at high pressure and the thermodynamic properties of corundum: Application of Kieffer's model, Am. Mineral. 80 (1995) 1157-1165. https://doi.org/10.2138/am-1995-11-1206

[40] S. Cava, S.M. Tebcherani, I.A. Souza, S.A. Pianaro, C.A. Paskocimas, E. Longo, J.A. Varela, Structural characterization of phase transition of Al_2O_3 nanopowders obtained by polymeric precursor method, Mater. Chem. Phys. 103 (2007) 394-399. https://doi.org/10.1016/j.matchemphys.2007.02.046

[41] K.S. Wan, S. Tochino, W.L. Zhu, S. Ohtsuka, G. Pezzotti, Quantitative evaluation of probe response functions for Raman and fluorescence bands of single-crystalline and polycrystalline Al_2O_3, J. Phys. D Appl. Phys. 43 (2010) 205501. https://doi.org/10.1088/0022-3727/43/20/205501

[42] J. Mougin, T. Le Bihan, G. Lucazeau, In situ Raman monitoring of chromium oxide scale growth for stress determination, J. Raman Spectrosc. 32 (2001) 739-744. https://doi.org/10.1002/jrs.734

[43] A.S.O. Gomes, N. Yaghini, A. Martinelli, E. Ahlberg, A micro- Raman spectroscopic study of $Cr(OH)_3$ and Cr_2O_3 nanoparticles obtained by the hydrothermal method, J. Raman Spectrosc. 48 (2017) 1256-1263. https://doi.org/10.1002/jrs.5198

[44] Q. Li, Y. Gou, T.-G. Wang, T. Gu, Q. Yu, L. Wang, Study on local residual stress in a nanocrystalline Cr_2O_3 coating by micro-Raman spectroscopy, Coatings 9 (2019) 500. https://doi.org/10.3390/coatings9080500

[45] A. Moustaghfir, E. Tomasella, M. Jacquet, A. Rivaton, B. Mailhot, J.L. Gardette, E. Bêche, ZnO/Al_2O_3 coatings for the photoprotection of polycarbonate, Thin Solid Films 515 (2006) 662-665 https://doi.org/10.1016/j.tsf.2005.12.234

[46] K. Djebaili, Z. Mekhalif, A. Boumaza, A. Djelloul, XPS, FTIR, EDX, and XRD Analysis of Al_2O_3 Scales Grown on PM2000 Alloy, J. Spectrosc. 2015 (2015) 1-16. https://doi.org/10.1155/2015/868109

[47] J. Colas, L. Charpentier, D. Chen, E. Bêche, J. Esvan, D. De Sousa Meneses, F. Mercier, M. Pons, M. Balat-Pichelin, Oxidation and high-temperature radiative properties of the Kanthal Super ER intermetallic alloy, Corros. Sci. 189 (2021) 109601. https://doi.org/10.1016/j.corsci.2021.109601

[48] M. Balat-Pichelin, E. Bêche, Atomic oxygen recombination on the ODS PM 1000 at high temperature under air plasma, Appl. Surf. Sci. 256 (2010) 4906-4914. https://doi.org/10.1016/j.apsusc.2010.03.002

[49] A. Wiatrowski, M. Mazur, A. Obstarczyk, D. Wojcieszak, D. Kaczmarek, J. Morgiel, D. Gibson, Comparison of the physicochemical properties of TiO_2 thin films obtained by magnetron sputtering with continuous and pulsed gas flow, Coatings 8 (2018) 412. https://doi.org/10.3390/coatings8110412

[50] V. Kumaravel, S. Rhatigan, S. Mathew, M.C. Michel, J. Bartlett, M. Nolan, S.J. Hinder, A. Gascó, C. Ruiz-Palomar, D. Hermosilla, S.C. Pillai, Mo doped TiO_2: impact on oxygen vacancies, anatase phase stability and photocatalytic activity, J. Phys. Mater. 3 (2020) 025008. https://doi.org/10.1088/2515-7639/ab749c

[51] V. Serin, E.Bêche, R. Berjoan, O. Abidate, D. Dorignac, D. Rats, J. Fontaine, L. Vandenbulcke, C. Germain, A. Catherinot, XAES, XPS, EELS and Raman spectroscopy of polycristalline to amorphous carbon films with various sp3 and sp2 bondings, Proc. of the Vth Int. Symp. on Diamond Materials, The Electrochemical Society, 97/32 (1998) 126-141.

[52] D. Briggs and M.P. Seah, Practical Surface Analysis, Auger and X-ray photoelectron spectroscopy, J. Wiley & Sons, New York, 1983.

[53] B. Gorr, F. Müller, S. Schellert, H.-J. Christ, H. Chen, A. Kauffmann, M. Heilmaier, A new strategy to intrinsically protect refractory metal based alloys at ultra high temperatures, Corros. Sci. 166 (2020) 108475. https://doi.org/10.1016/j.corsci.2020.108475

[54] S. Schellert, M. Weber, H.J. Christ, C. Wiktor, B. Butz, M.C. Galetz, S. Laube, A. Kauffmann, M. Heilmaier, B. Gorr, Formation of rutile $(Cr,Ta,Ti)O_2$ oxides during oxidation of refractory high

entropy alloys in Ta-Mo-Cr-Ti-Al system, Corros. Sci. 211 (2023) 110885. https://doi.org/10.1016/j.corsci.2022.110885

[55] H. Aréna, M. Coulibaly, A. Soum-Glaude, A. Jonchère, G. Arrachart, A. Mesbah, N. Pradeilles, M. Vandenhende, A. Maître, X. Deschanels, Effect of TiC incorporation on the optical properties and oxidation resistance of SiC ceramics, Sol. Energ. Mat. Sol. C.213 (2020), 110536. https://doi.org/10.1016/j.solmat.2020.110536

[56] L. Charpentier, F. Mercier, D. Chen, E. Bêche, C. Escape, M. Balat-Pichelin, High temperature oxidation of SiC-coated Fe-Cr-Al-Mo alloys in muffle and concentrated solar furnaces, Thin Solid Films 763 (2022) 139564. https://doi.org/10.1016/j.tsf.2022.139564

[57] Y.S. Touloukian, D.P. DeWitt, Thermophysical Properties of Matter, Volume 8 – Thermal Radiative Properties, Nonmetallic Solids, IFI/Plenum, New York-Washington, 1972.

List of Figure captions

Figure 1. Normal spectral emissivity at room temperature of a) MST b) TMCA c) TMCTA. The emissivities are compared to the ones of oxidized Inconel 625 previously measured [4].

Figure 2. Calculated solar absorptivity α before and after 6h oxidation in air at 1100 °C of a) MST b) TMCA c) TMCTA d) Inconel 625 (from [4])

Figure 3. XRD diffractograms of MST, oxidized during 6h in air at 1100 °C

Figure 4. Optical images (a; c) and associated µ-Raman spectrum (b; d) on MST, as-polished (a-b) and oxidized during 6h in air at 1100 °C (c-d).

Figure 5. Deconvolution of the O 1s spectrum of the XPS profile of the oxidized MST sample.

Figure 6. Results from the optical roughness measurement: 1× 1 mm^2 surfaces of the MST sample, a) polished and b) polished then oxidized during 6h in air at 1100°C, and the associated average arithmetic (Sa) and quadratic (Sq) surface roughnesses measured from five different surfaces, with the corresponding standard deviations.

Figure 7. XRD diffractograms of TMCA (a) and TMCTA (b), oxidized during 6h in air at 1100 °C.

Figure 8. Optical images (a; c) and associated µ-Raman spectrum (b; d) on oxidized TMCA, analysis on the characteristic image (a-b) and point analysis on yellow grains (c-d).

Figure 9. Optical images (a; c) and associated µ-Raman spectrum (b; d) on oxidized TMCTA, analysis on the characteristic image (a-b) and analysis on minor yellow-white areas c-d).

Figure 10. Deconvolution of the O 1s spectrum of the XPS profile of the oxidized TMCA (a: point 2) and TMCTA (b: point 1, c: point 2) sample.

Figure 11. Results from the optical roughness measurement: 1× 1 mm^2 surfaces of the TMCA (a-b) and TMCTA (c-d) samples, polished (a ; c) and polished then oxidized during 6h in air at 1100°C (c ; d), and the associated average arithmetic (Sa) and quadratic (Sq) surface roughnesses measured from five different surfaces, with the corresponding standard deviations.

Figure 12. Values of normal spectral reflectance of polycrystalline Al_2O_3, Cr_2O_3, SiO_2 and of rutile TiO_2, extracted from literature database [50]

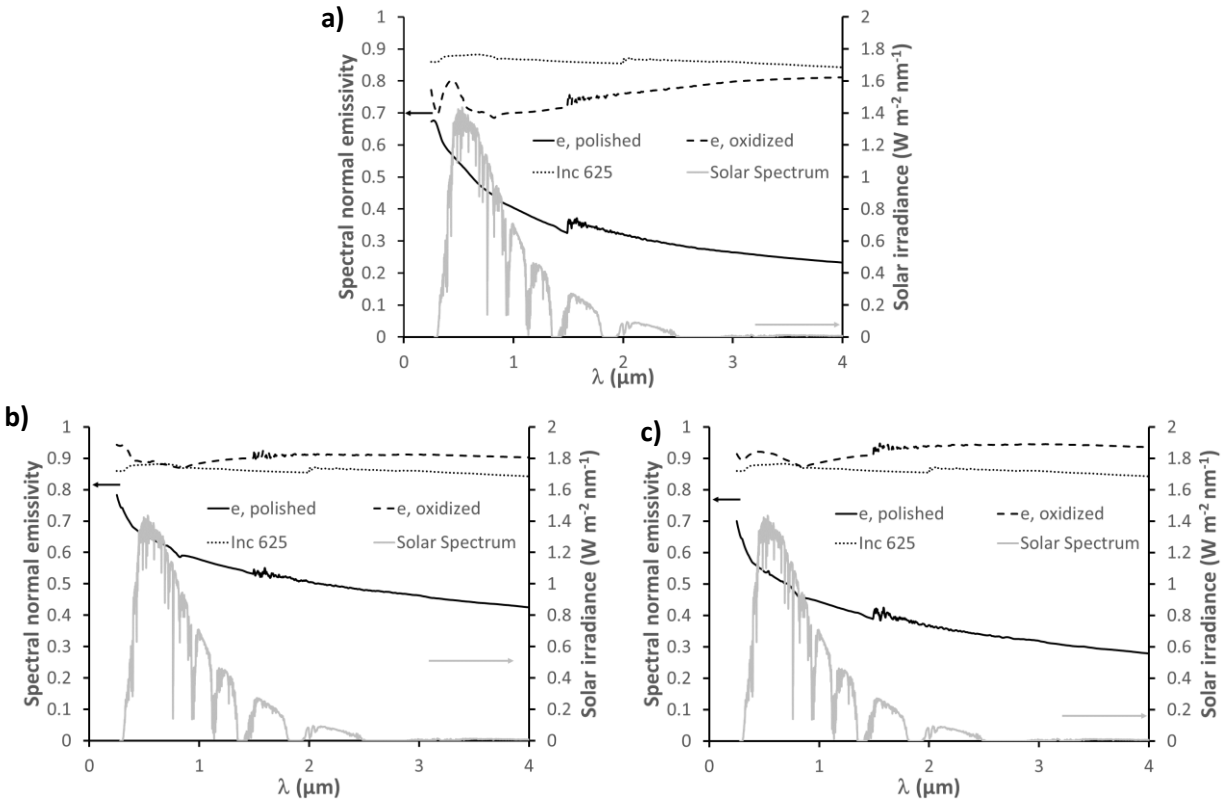
a)
b)
c)
Spectral normal emissivity
Solar irradiance (W m-2 nm-1)
λ (μm)
e, polished
e, oxidized
Inc 625
Solar Spectrum

Figure 1.

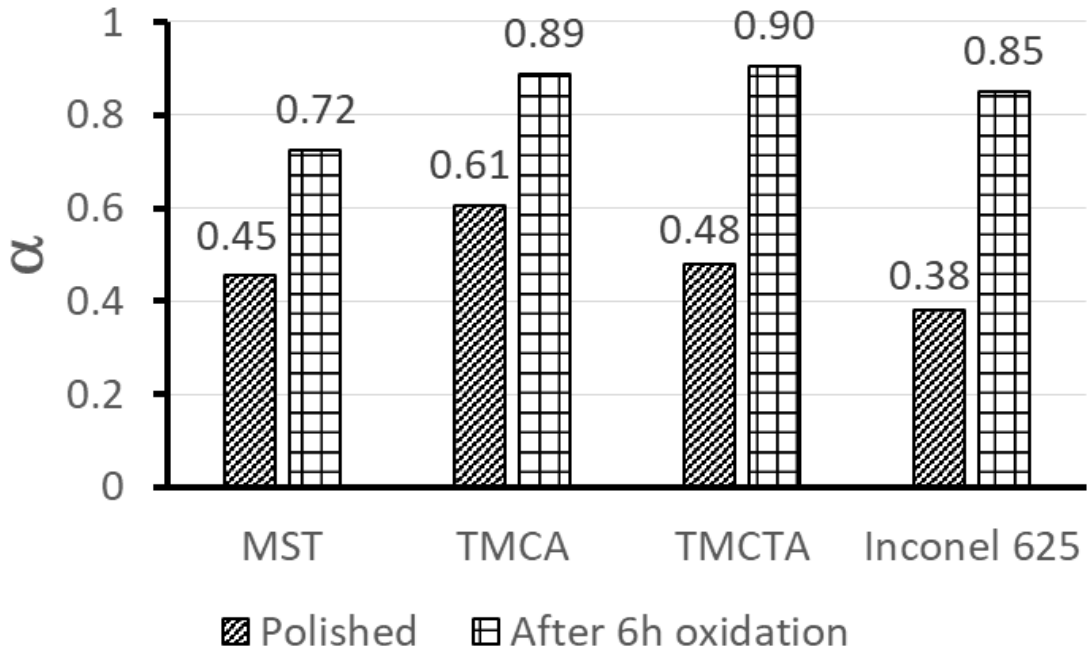
1
0.8
0.6
0.4
0.2
0
α
0.45
0.72
0.61
0.89
0.48
0.90
0.38
0.85
MST
TMCA
TMCTA
Inconel 625
Polished
After 6h oxidation

Figure 2.

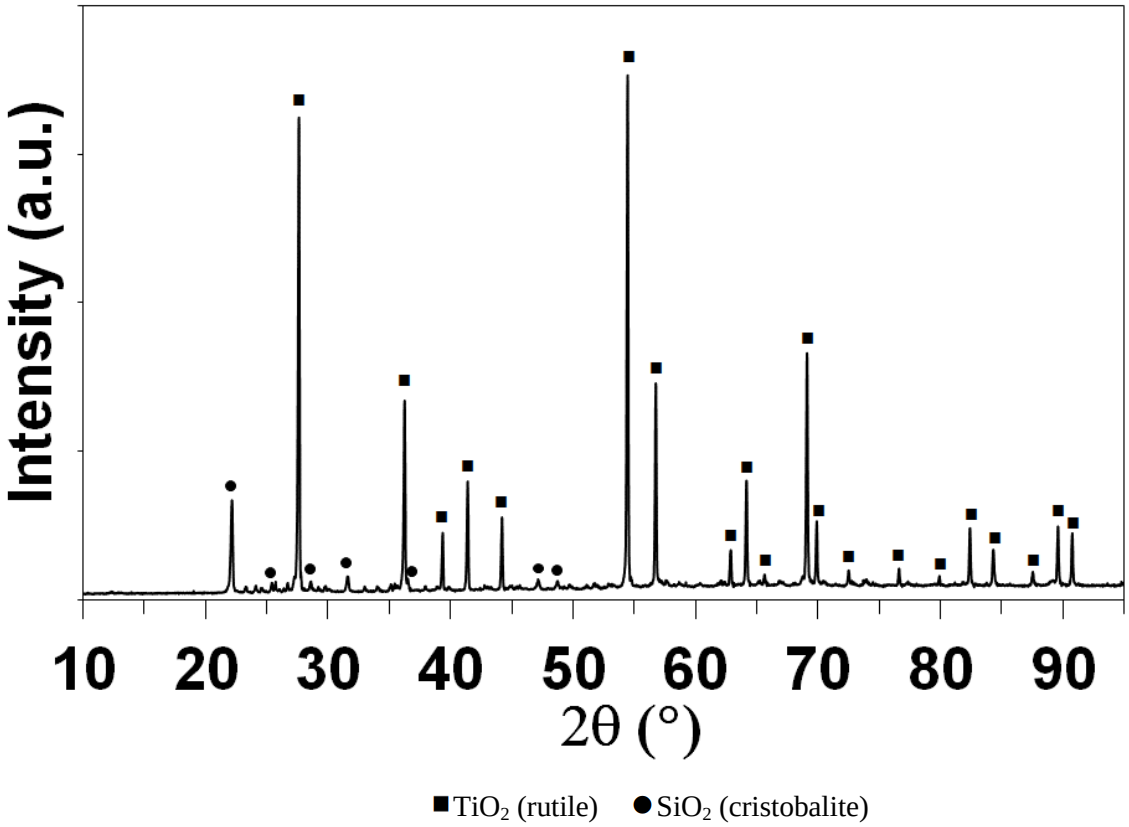
Intensity (a.u.)
10
20
30
40
50
60
70
80
90
2θ (°)
■TiO2 (rutile)
●SiO2 (cristobalite)

Figure 3.

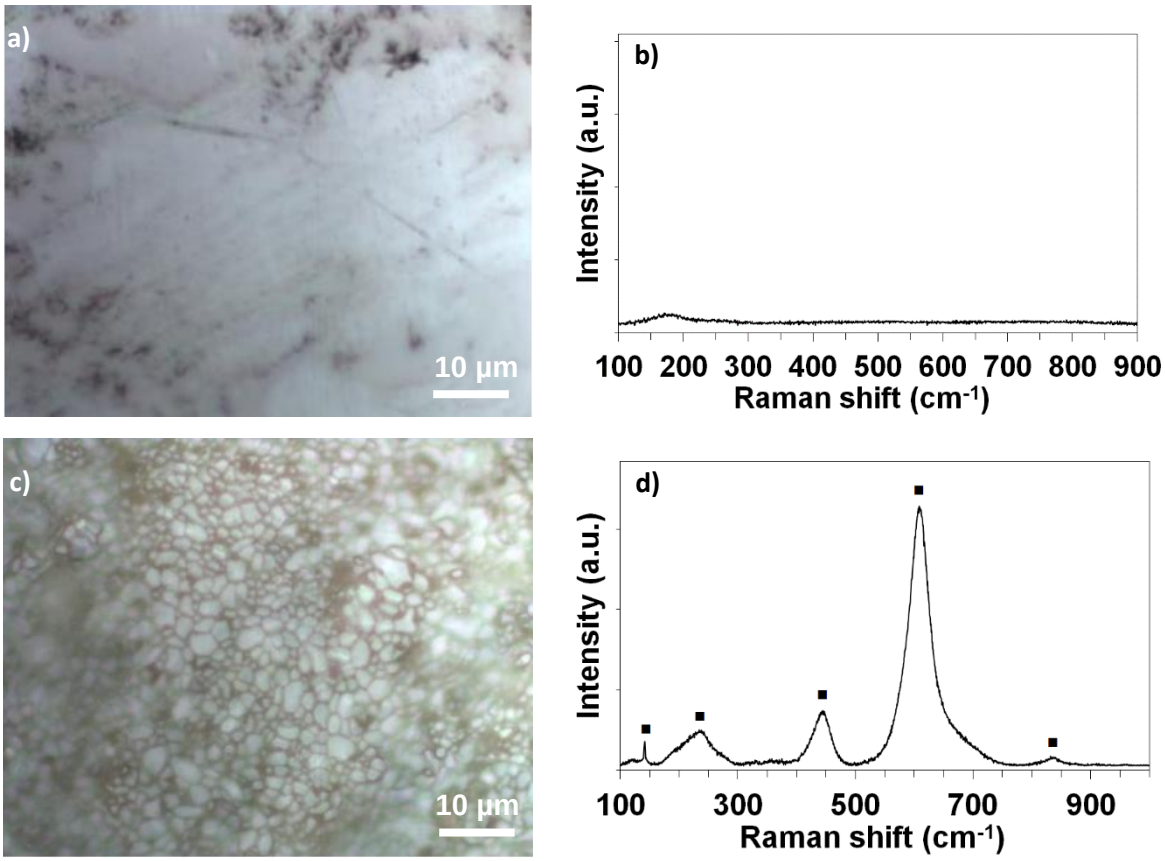
a)
10 µm
b)
Intensity (a.u.)
100 200 300 400 500 600 700 800 900
Raman shift (cm-1)
c)
10 µm
d)
Intensity (a.u.)
100 300 500 700 900
Raman shift (cm-1)

Figure 4.

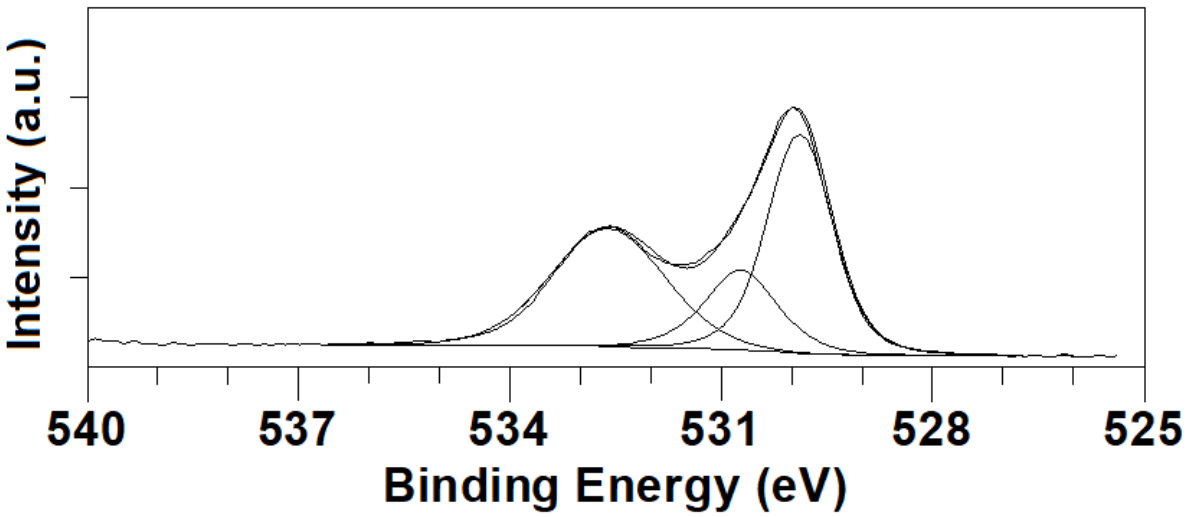

Figure 5.

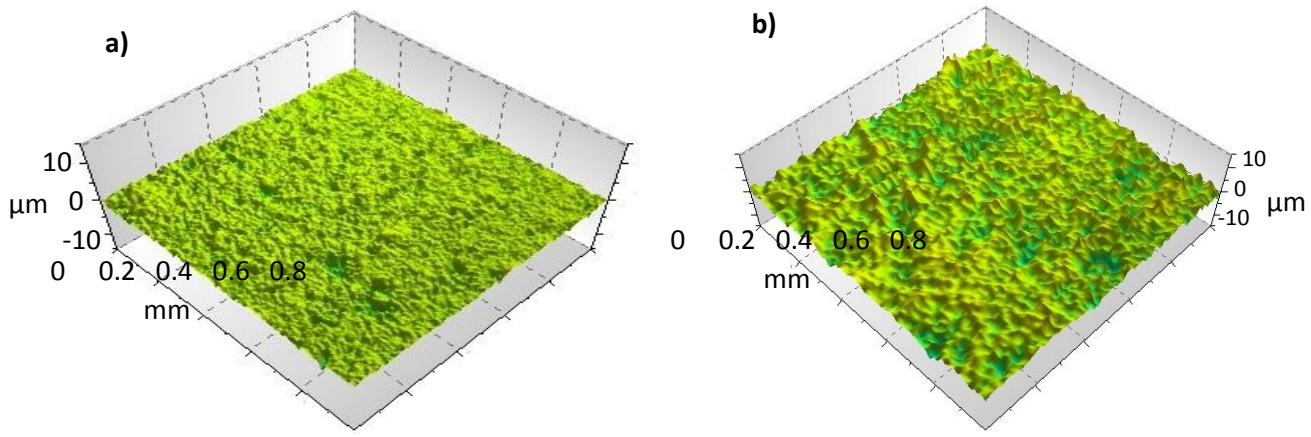

Sa = (0.36 ± 0.12) µm

Sq = (0.55 ± 0.19) µm

Sa = (1.46 ± 0.32) µm

Sq = (2.05 ± 0.52) µm

Figure 6.

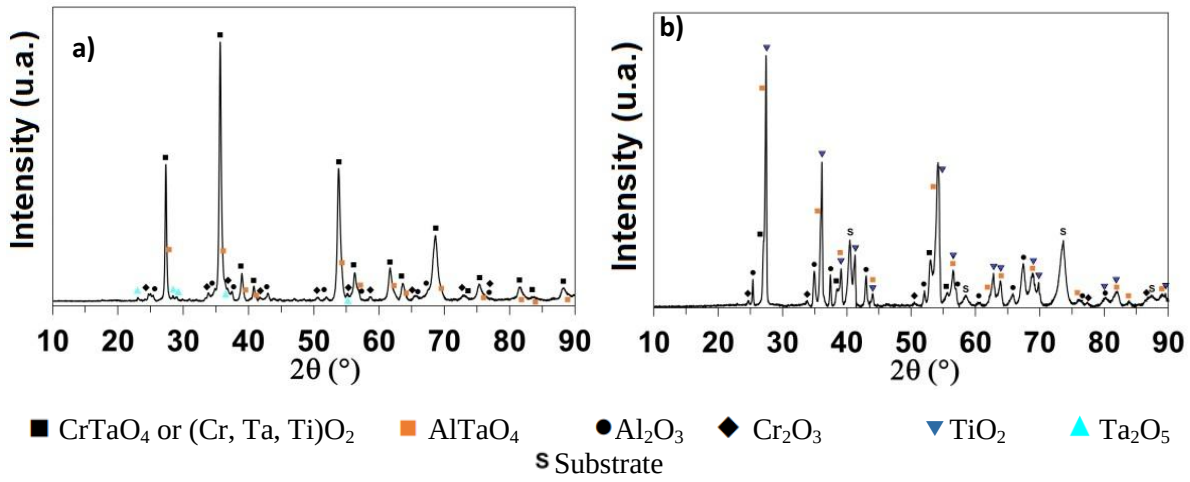
a)
b)
Intensity (u.a.)
Intensity (u.a.)
10 20 30 40 50 60 70 80 90
2θ (°)
10 20 30 40 50 60 70 80 90
2θ (°)
■ CrTaO4 or (Cr, Ta, Ti)O2
■ AlTaO4
● Al2O3
◆ Cr2O3
▼ TiO2
▲ Ta2O5
S Substrate

Figure 7.

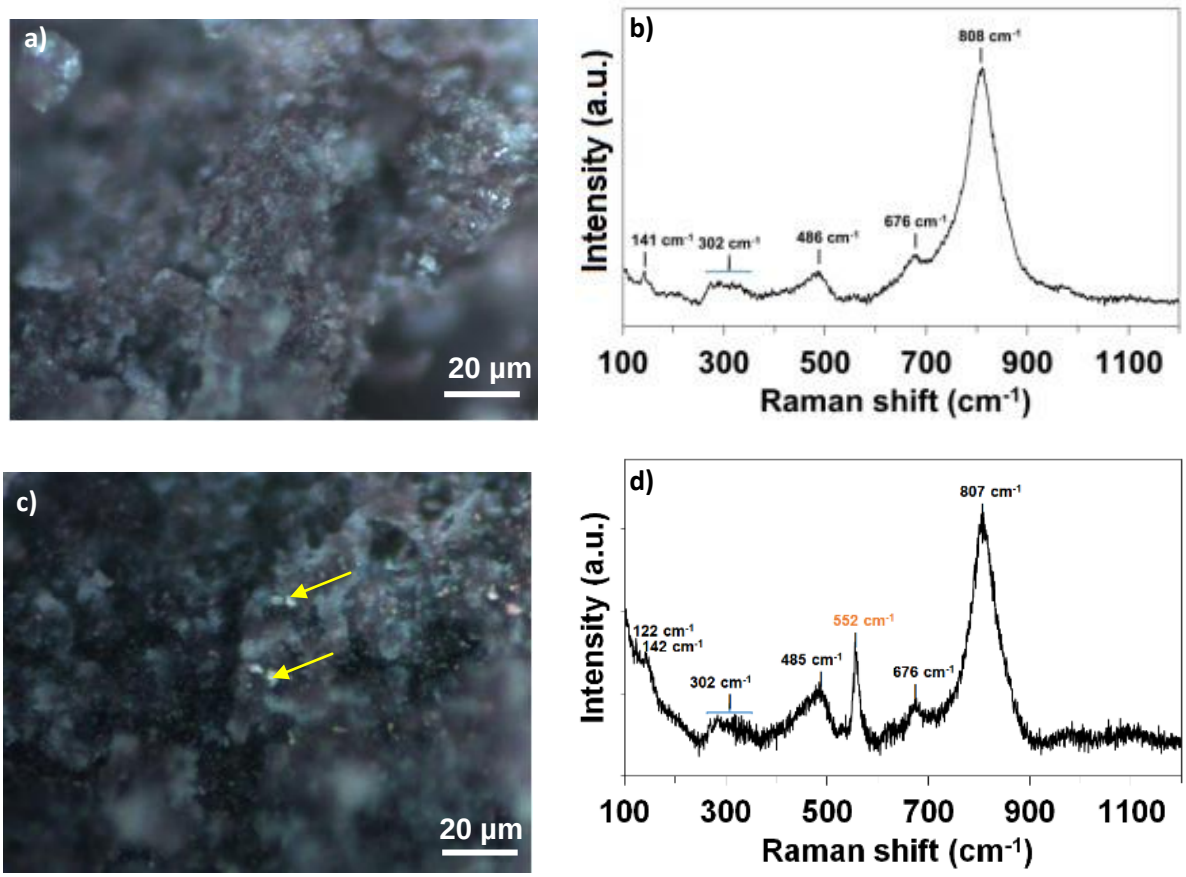
a)
20 μm
b)
808 cm-1
Intensity (a.u.)
141 cm-1
302 cm-1
486 cm-1
676 cm-1
100
300
500
700
900
1100
Raman shift (cm-1)
c)
20 μm
d)
807 cm-1
Intensity (a.u.)
122 cm-1
142 cm-1
552 cm-1
485 cm-1
302 cm-1
676 cm-1
100
300
500
700
900
1100
Raman shift (cm-1)

Figure 8.

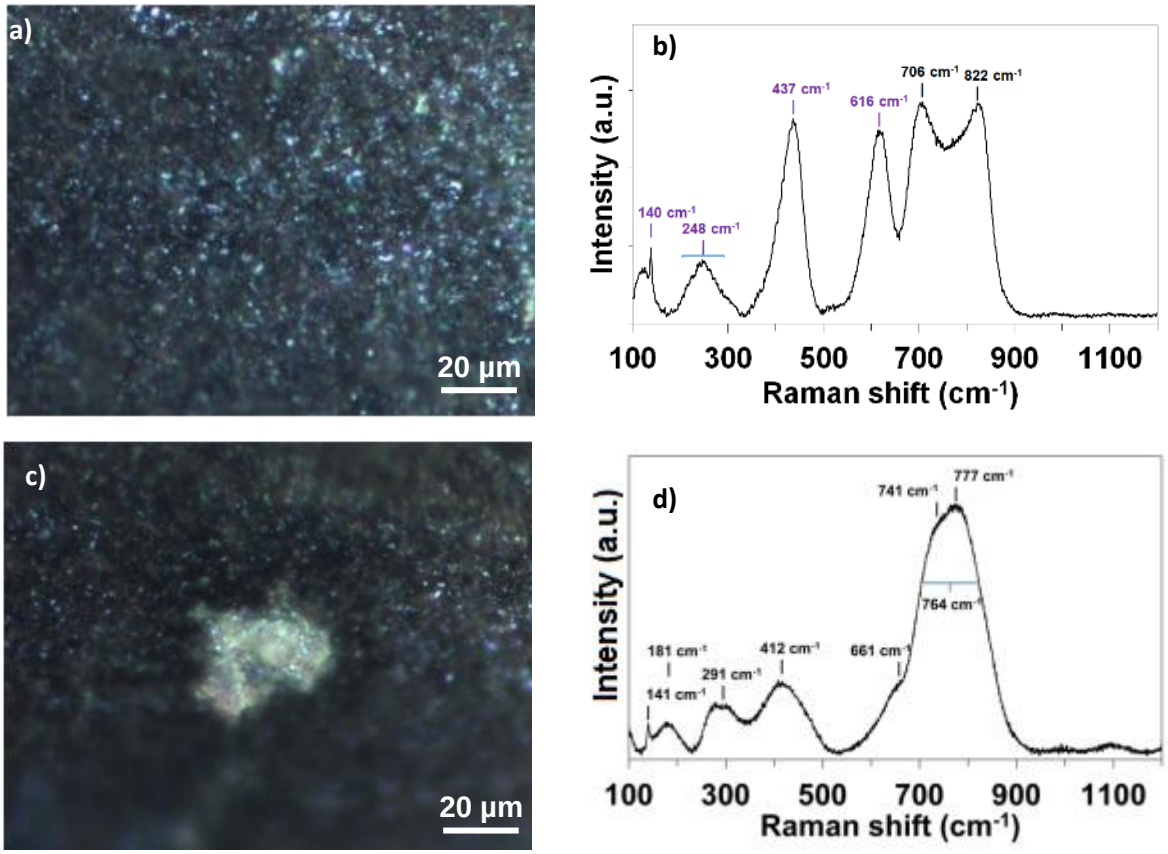
a)
20 μm
b)
Intensity (a.u.)
140 cm-1
248 cm-1
437 cm-1
616 cm-1
706 cm-1
822 cm-1
100
300
500
700
900
1100
Raman shift (cm-1)
c)
20 μm
d)
Intensity (a.u.)
141 cm-1
181 cm-1
291 cm-1
412 cm-1
661 cm-1
741 cm-1
764 cm-1
777 cm-1
100
300
500
700
900
1100
Raman shift (cm-1)

Figure 9.

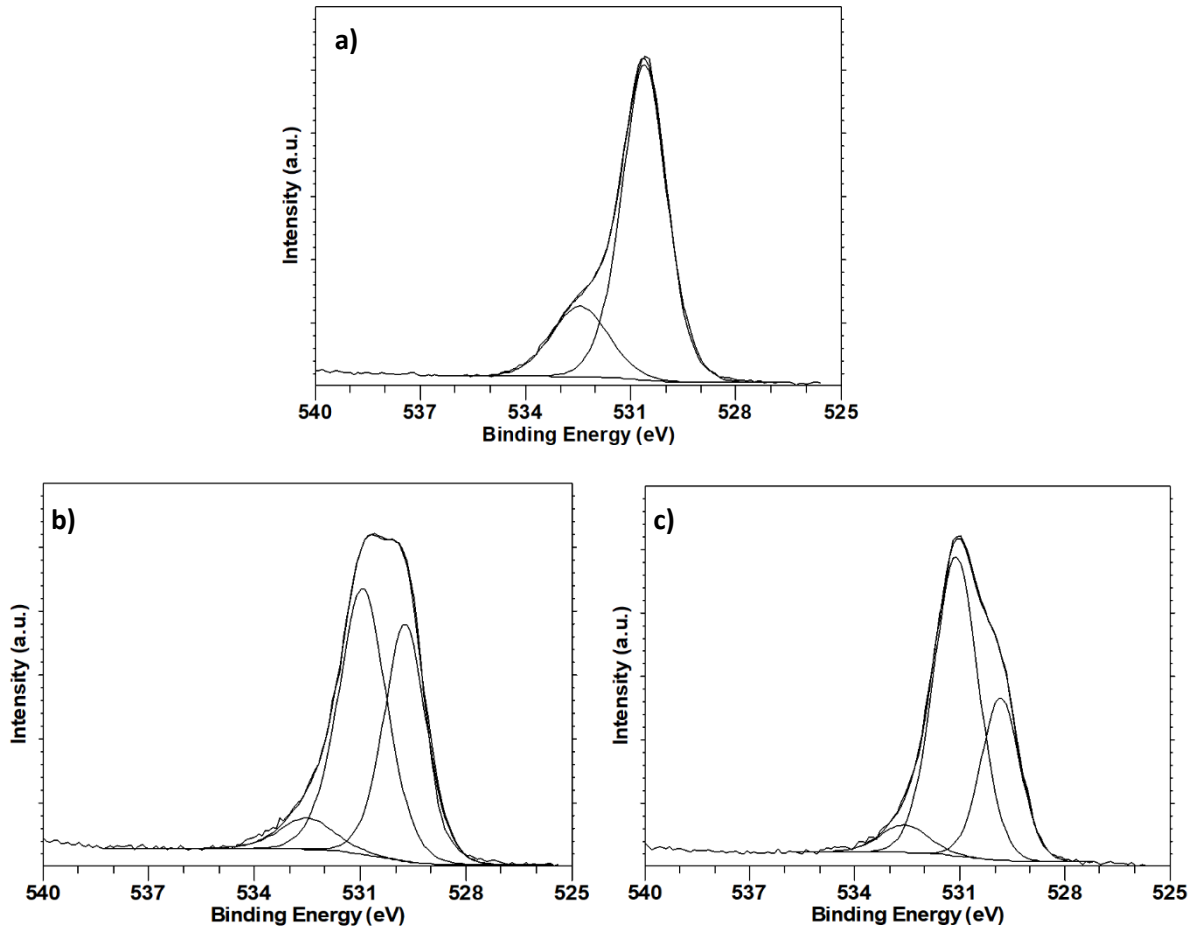
a)
Intensity (a.u.)
540
537
534
531
528
525
Binding Energy (eV)
b)
Intensity (a.u.)
540
537
534
531
528
525
Binding Energy (eV)
c)
Intensity (a.u.)
540
537
534
531
528
525
Binding Energy (eV)

Figure 10.

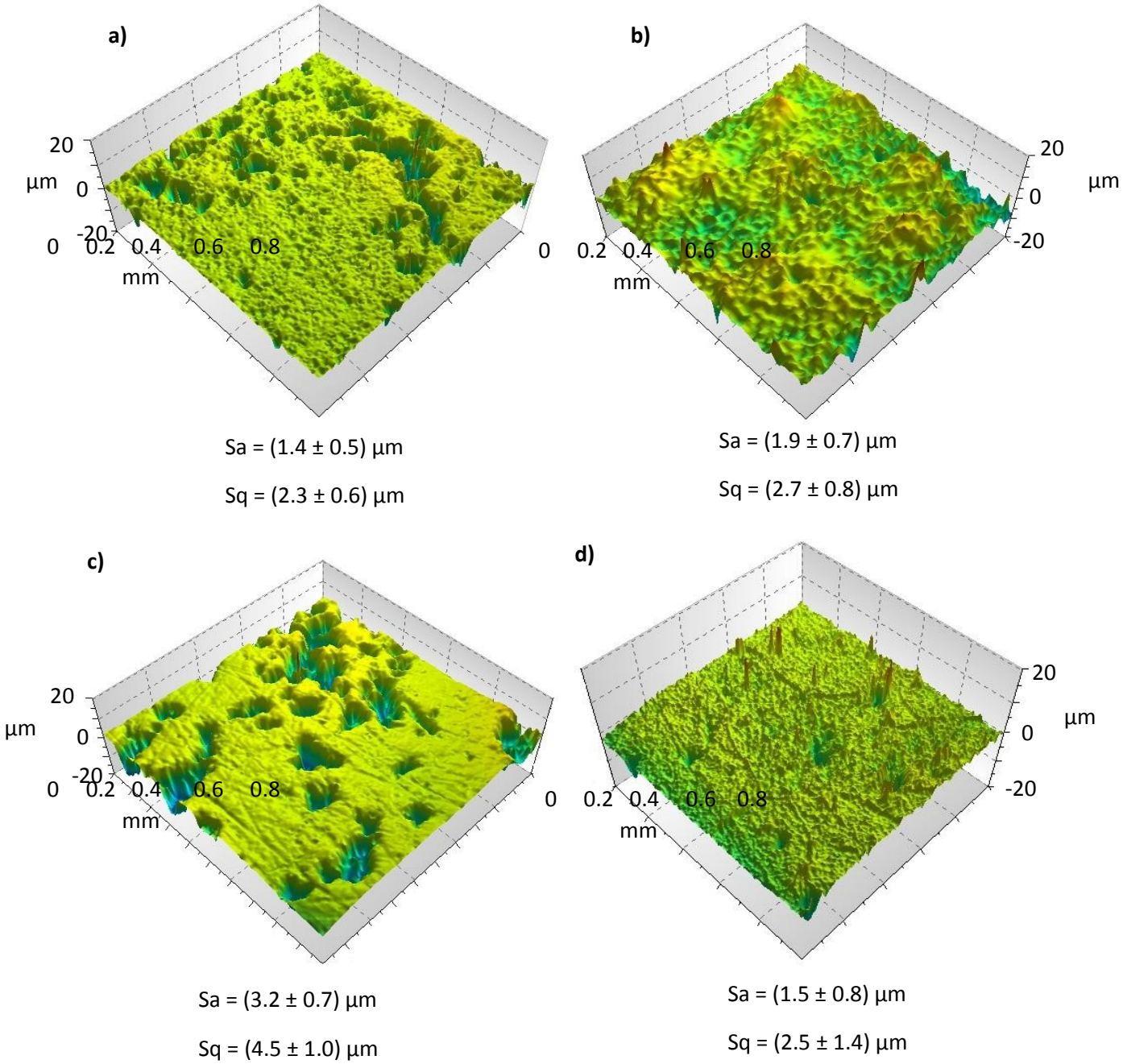

Sa = (1.4 ± 0.5) µm

Sq = (2.3 ± 0.6) µm

Sa = (1.9 ± 0.7) µm

Sq = (2.7 ± 0.8) µm

Sa = (3.2 ± 0.7) µm

Sq = (4.5 ± 1.0) µm

Sa = (1.5 ± 0.8) µm

Sq = (2.5 ± 1.4) µm

Figure 11.

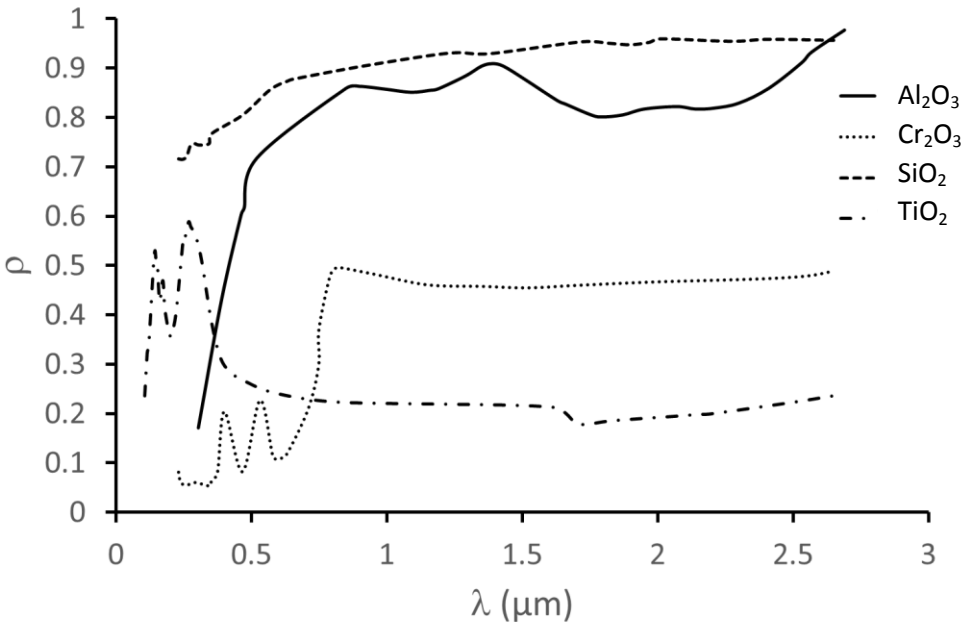
1
0.9
0.8
0.7
0.6
0.5
0.4
0.3
0.2
0.1
0
ρ
0
0.5
1
1.5
2
2.5
3
λ (μm)
Al2O3
Cr2O3
SiO2
TiO2

Figure 12.